Hetero-structured Approaches to Efficient Thermoelectric Materials

Yichi Zhang[†] and Galen D. Stucky[†, §,*]

[†]Department of Chemistry and Biochemistry, University of California, Santa Barbara CA 93106-9510
[§]Materials Department, University of California, Santa Barbara, California CA 93106-5050

KEYWORDS Hetero-structures, Thermoelectric Materials, Nano-inclusions, Metal-semiconductor, Interfacial Barrier, Hot Carrier Filtering

ABSTRACT: A key challenge for the materials chemist is the development of controllable and straightforward synthetic methodologies that will integrate multiple phases/compositions with scalar designed physical properties. The intent of this review is to give a brief summary of some of the current bulk-scaled approaches that might help guide researchers in the design of optimal hetero-structures in large quantity for the further improvement of thermoelectric conversion efficiency. Examples of two-phase combinations on different length scales will be discussed with a focus on the hot carrier filtering effect that results from the selective scattering of carriers with different energies. Based on this strategy, hetero-structures fabricated by both the bottom-up solution approaches at low temperature and top-down solid-state deposition routes that show promise in improving the thermoelectric figure of merit are highlighted, which may help guide researchers in the design of novel hetero-structures for further improvement.

1. Introduction

1.1 Thermoelectric materials

Thermoelectric (TE) materials interchange thermal energy and electricity for the utilization of waste heat and for cooling. In either case an inexpensive and scalable TE material with a high energy-conversion performance is highly desired. The upper limit of the TE conversion efficiency is defined by the Carnot efficiency. **Figure 1(a)** shows the energy conversion efficiency accomplished by TE materials with different zT values across a Carnot temperature gradient, in which zT is the dimensionless figure of merit as defined in **E1**.

$$zT = S^2\sigma T/\kappa \qquad (E1)$$

This equation allows designers to control the parameters, including Seebeck coefficient (S), electrical conductivity (σ) and thermal conductivity (κ), of materials to optimize performance. However, for single-phase materials, the biggest challenge in improving the figure of merit lies in the inter-dependence of each variable in E1. As illustrated in Figure 1(b),[1] the Seebeck coefficient (S) decreases as the carrier density increases while the other two parameters, electrical conductivity (σ) and thermal conductivity (κ), increase when the carrier density increases. The maximum zT fits into the degenerate semiconductor range with an optimal carrier density from $10^{19}/cm^3$ to $10^{21}/cm^3$.[1,2] The figure of merit and the power efficiency are therefore limited by this variable inter-dependence. The consequence of this physics is that for the single-phase thermoelectric materials that have been synthesized and studied over the past 150 years,[3,4] the TE power efficiency has been limited to 5% or less for low-temperature applications (< 400 K) and to ~ 15% or less at high temperatures (900 K or greater).

A solution to this impasse is to synthesize thermoelectric materials that are hierarchically defined by the length scales of the property variables given in equation E1. However, as illustrated in Figure 1(b), two pairs of variables with conflicting dependence exist in a typical single-band electron system: electrical conductivity and thermal conductivity; and, Seebeck coefficient and electrical conductivity. A successful TE material is expected to maximize one variable without degrading the other one in the conflicting pairs. More specifically, decoupling the electrical and thermal conductivity along with enhancement of the Seebeck coefficient while simultaneously retaining or increasing the electrical conductivity is required. In addition to this, a scalable methodology that is able to produce the thermoelectric system in large quantities at low cost is necessary for practical applications. This is because the heat flux along a bar of length L is proportional to $(T_H - T_L)/L$ so that the temperature gradient across a bulk module is larger than that in a small-scaled device, resulting in a higher power efficiency as illustrated in Figure 1(a).

In this review, the emphasis will be on bulk scaled approaches for the synthesis of hetero-structures that

target the successful simultaneous decoupling of those variables. Ideally we wish to use a bottom-up chemistry approach to generate property-defined phase separation of multi-components on multiple length scales in order to create bulk thermoelectric systems.

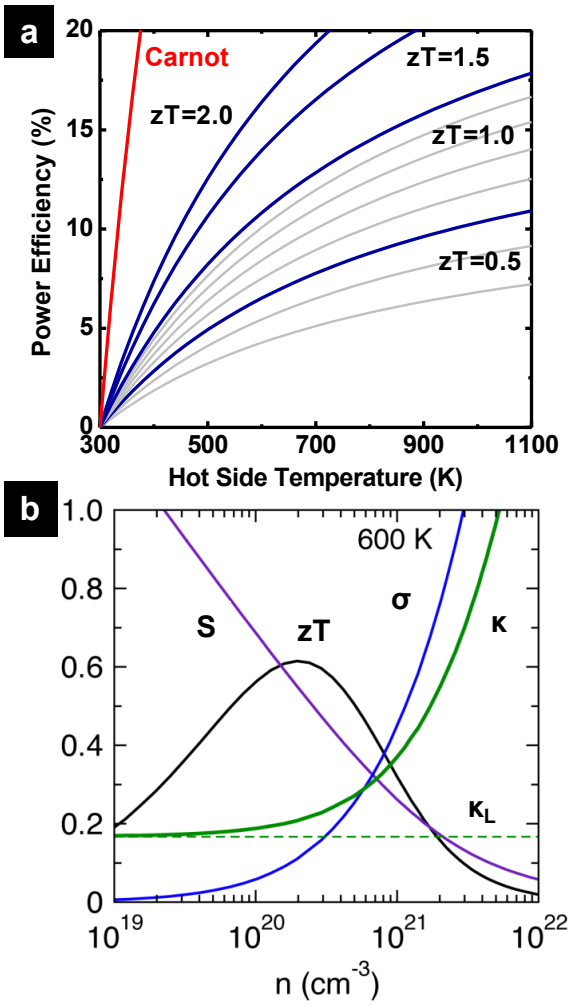

Figure 1. (a) Power generator efficiency as a function of temperature gradient for a material with different zT value from 0.5 to 2.0. The heat sink temperature is assumed to be 300 K. (b) Optimizing zT through carrier concentration tuning. Curves are based on results from a $Ba_8Ga_{16-x}Ge_{30+x}$ sample with $n = 8\times10^{20}$ cm^{-3} at 600 K generated with a single parabolic band model. The value of 1 on the y-axis corresponds to zT = 1; S = 400 μV/K; $\sigma = 2\times10^5$ S/m and κ = 5 W/(m·K). (b) is reprinted with permission from ref. 1. Copyright 2010 American Chemical Society.

1.2 Single-compositional phase nanostructured alloys

Alloyed nanostructures have been demonstrated to successfully decouple the electrical and thermal conductivity by efficiently scattering phonons rather than electrons.[5–12] These alloyed nanostructures include nanocomposites made up of nanoparticles that are prepared by either top-down[5–8] or bottom-up[9–12] strategies and nanoporous composites such as porous membranes[13] and 3-dimensional porous monoliths.[14] A substantial reduction in thermal conductivity can take advantage of both atomic defects in the lattice that are the result of 1) alloyed atomic substitution along with 2) grain boundaries that are part of the hierarchical length scale necessary to completely cover the entire phonon mean free path (MFP) distribution range in the material system. As shown in **Figure 2**, the relative reduction in thermal conductivity of silicon nanowires (Si NWs) by alloy scattering as well as boundary scattering was quantified by Dames and Chen.[15–17] For this system, introducing defects that are of the appropriate dimensions to scatter phonons in the property length scale of a few nm to 1 μm is highly desirable in order to maximize the phonon scattering and thereby reduce the thermal conductivity. However, due to the narrow phonon MFP distribution in other material systems, such as telluride compounds, using this strategy to produce an ideal hierarchical structure with a high degree of atomic ordering to maximize electron transport and appropriately dimensioned longer-range lattice defects to maximize phonon scattering is a formidable challenge, especially for single-phase alloy nanostructures. Therefore, the most encouraging recent breakthrough (a state-of-the-art zT value of 2.2 in a PbTe based material system) in the thermoelectric field came from a hierarchical hetero-structure containing SrTe nano-inclusions instead of a single compositional phase material.[18]

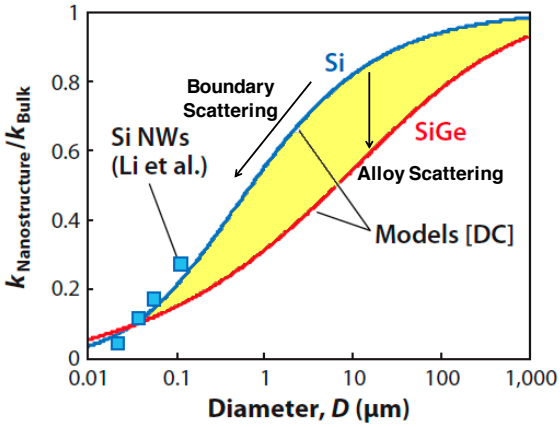

Figure 2. Calculated (*lines*) and measured (*points*) thermal conductivity of Si and SiGe nanowires at 300 K. Sources: [DC] = Dames & Chen;[16] [Li *et al.*].[17] The yellow area indicates the relative reduction by introducing germanium substitutions. Adapted with permission from ref. 15. Copyright 2012 Annual Reviews.

1.3 Multi-phased hetero-structures

1.3.1 Advantages of hetero-structures in theory

Taking the structure in ref. 18 as one example, we define a structure containing identifiable composition(s) or phase(s) that is(are) integrated within the majority composition or phase and are distinguishable from that majority component as a hetero-structure system. The state-of-the-art zT value of 2.2 in the PbTe-based material system[18] resulted from the creation of a second integrated

nanostructured phase with inherent different property length scales resulting from atomic doping and the creation of grain boundaries. This much more completely covered the phonon MFP distribution range and gave a thermoelectric efficiency that was substantially better than simpler single-phased nanostructures with related chemical compositions.[18]

In addition, the incorporation of multi-phases provides an opportunity to produce a unique electron (carrier) transport behavior that can be used to decouple electron transport from the phonon scattering at the interfaces. This is important since there is limited room for further reduction of thermal conductivity without losing electrical conductivity. In general, the heat transport relies on the electronic carriers as well as the lattice vibrations of the crystal, which means that the two types of conductivities (σ and κ) are naturally coherent with each other. This coherence can be understood quantitatively by **E2**, in which the total thermal conductivity (κ) is split into two parts: lattice contribution and electronic contribution. According to the Wiedemann-Franz law, the latter contribution is related to the electrical conductivity (σ) with a factor of Lorentz number (L) and temperature (T).

$$\kappa = \kappa_L + \kappa_e = \kappa_L + L\sigma T \qquad (E2)$$

This relation means that any reduction in κ_e will result in a reduction in electrical conductivity. The desired strategy is to reduce the lattice contribution (κ_L) without affecting the electronic part. However, in general, the lattice contribution cannot be reduced below the amorphous limit. One notable exception is the ultra-low thermal conductivity found in disordered, layered WSe_2, TE material systems.[19] What is more likely to be found is exemplified by the experimentally measured lattice thermal conductivity of the nanocomposite made up of ball-milled nanoparticles of p-type Bi_2Te_3,[5] which approaches the amorphous limit of Bi_2Te_3 as calculated using Cahill's model.[20]

This result makes obvious the importance of introducing further improvement in thermoelectric efficiency and zT by decoupling the variables (S and σ). Conceptually this relies on the energy-dependent scattering of electrons (carriers) at interfaces, which can be accomplished in hetero-structures with interfacial band offset or bending. This carrier transport behavior, or so called hot-carrier filtering effect in hetero-structures has been theoretically studied for several model structures.[21–26] Specifically, superlattice structures, an integration of multiple semiconductor phases, have been defined with an interfacial band offset in order to selectively scatter out the low-energy carriers. While the low-energy carriers are being scattered, the high-energy carriers can transport over an energy barrier as illustrated in **Figure 3(a)**.[22] In contrast to the first category described above that involves semiconducting phase combinations, metal-semiconductor hetero-structures define the second group of hetero-structures.[23,24,26] In this group, band bending at the metal-semiconductor contact plays an important role in highlighting the differential transport behaviors of the carriers with different energies.

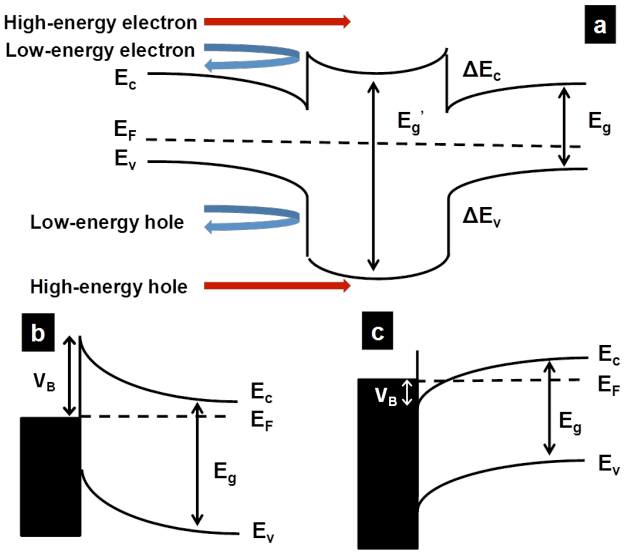

Figure 3. (a) Schematic of the of the band structure of filtering effect. Here E_c (E_v) is the conduction (valence) band edge and ΔEc (ΔEv) is the conduction (valence) band edge difference of two materials. E_g (E_g') is the band gap of the matrix material (second phase). Low-energy carriers are scattered more than the high-energy carriers over the energy barrier; (b), (c) Schematic of the metal-semiconductor band alignments between n-type semiconductor and metals for Schottky contact (b) and Ohmic contact (c). VB is the interfacial barrier with positive (negative) sign in (b)((c)).[22]

As shown in Figure 3(b) and (c), two types of band bending can be formed at the metal-semiconductor interfaces: (b) is the case of a Schottky contact with positive interfacial potential while (c) shows an Ohmic contact with negative potential. According to Faleev's calculation,[24] the sign of the interfacial potential (V_B), positive or negative, which corresponds to the type shown in (b) or (c), does not affect either the Seebeck value or the mobility. This is primarily because in this band-bending potential, the scattering occurs mostly as a result of the spatially slowly varying potential (band-bending), rather than the sharp step-like potential V_B at the interface. This slowly varying potential is very strong for low-energy electrons, so that the scattering time increases with increasing energy. This scattering changes the total energy-dependent scattering time in the material, thus enhancing the Seebeck coefficient. This mechanism can be considered as a partial electron filtering effect. The key factor is the barrier height: the absolute value of the potential ($|V_B|$) must be optimized in order to maximize the enhancement in Seebeck coefficient and power factor ($S^2\sigma$) as shown in **Figure 4**.[24]

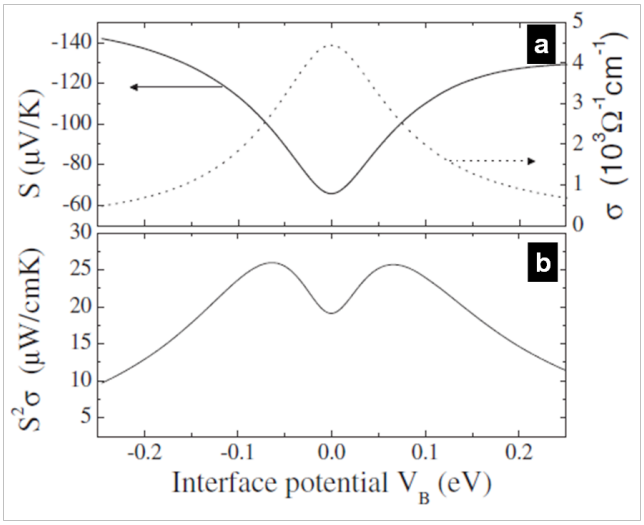

Figure 4. (a) Calculated Seebeck coefficient and conductivity for PbTe as a function of the interface potential V_B; (b) the resulting power factor. Parameters are metallic nanoparticle diameter d = 3 nm, temperature T = 300 K, volume fraction x = 5%, and carrier density n = 2.5×10^{19} cm^{-3}. Reprinted with permission from ref. 24. Copyright 2008 American Physical Society.

In this prediction, taking the material system of a metal phase-PbTe hetero-structure as an example, the optimal potential is ~ 0.1 eV.[24] However, in Faleev's calculation, a high volume fraction of nano-inclusions of 5% is included so that the nano-inclusions change the band structure of the matrix itself, which was not taken into account. This may result in an inaccurate result, as predicted by Zebarjadi *et al.*[27] Generally, relatively large nanoparticles with a proper band bending are considered to be useful in partially realizing electron filtering. In order to simplify the interpretation of the hot carrier filtering effect, the Mott expression (**E3**) is used,

$$S = \frac{\pi^2 k_B^2}{3q} T \left\{ \frac{d[\ln(\sigma(E))]}{dE} \right\}_{E=E_F} = \frac{\pi^2 k_B^2}{3q} T \left\{ \frac{d\,n(E)}{n\,dE} + \frac{d\mu(E)}{\mu\,dE} \right\}_{E=E_F} \quad (E3)$$

In it, the Seebeck coefficient (S) depends on the energy derivative of the energy-dependent electrical conductivity $\sigma(E) = n(E)\cdot e(E)\cdot\mu(E)$ taken at the Fermi (E_F) level. In this expression, $\mu(E)$ is the mobility, k_B is the Boltzmann constant, and q is electron charge. The term, $d\mu(E)/dE$, which is the energy derivative of the carrier mobility in the Mott expression can be enhanced if an appropriate barrier exists. In other words, the carriers' transport depends on their own energies.

1.3.2 Thin-film hetero-structures fabricated by high vacuum deposition

Experimentally, these theoretical predictions have been observed in some hetero-structures grown using high vacuum techniques such as molecular-beam epitaxy (MBE).[28] One successful demonstration is based on the MBE-grown III-V semiconductor superlattice, $In_{0.53}Ga_{0.47}As$/ $In_{0.53}Ga_{0.28}Al_{0.19}As$.[28] In this case, these two compositions were selected because the barrier height (V_B) between them was confirmed to be 200 meV. According to the theoretical simulations and experimental observations, the cross-plane Seebeck value is about two to three times higher than the in-plane Seebeck coefficient as shown in **Figure 5**,[28] which is mainly due to the hot electron filtering that occurs in the cross-plane direction rather than in the in-plane direction, since the interfacial barriers are uniaxial in the cross-plane direction. As a result, the zT value of this III-V superlattice is ~1.5 at 900 K.

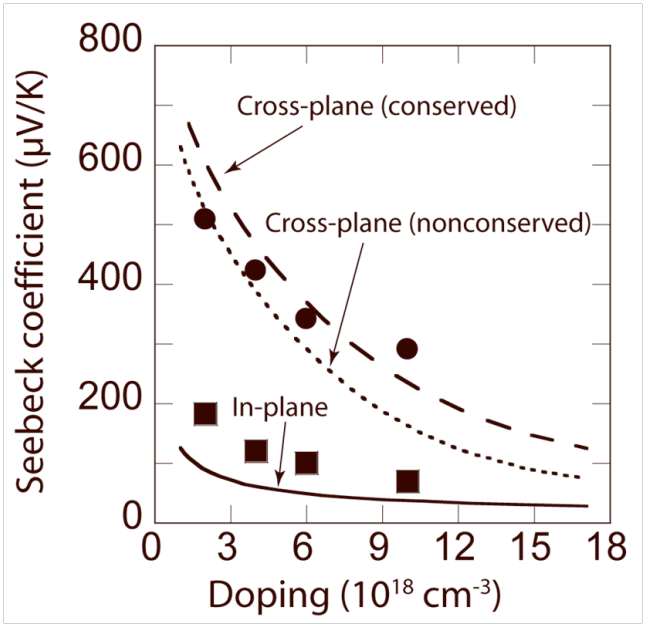

Figure 5. Room-temperature Seebeck coefficient; comparison of experimental and theoretical data in the in-plane direction (experimental data: squares, theory: solid curve) and cross-plane direction (experimental data: circles, theory: dashed curve for a superlattice with conserved transverse momentum and dotted curve for a superlattice with nonconserved transverse momentum). Experimental results indicate an improvement in the Seebeck coefficient due to electron filtering and a maximum zT value is ~1.5 at 900 K. Reprinted with permission from ref. 28. Copyright 2006 American Physical Society.

Similarly to this demonstration, some other thin films with hetero-structures, Te nanoparticle-dispersed $Bi_{0.5}Sb_{1.5}Te_3$[29,30] and a misfit layered compound $[(PbSe)_{0.99}]_m(WSe_2)_n$[31,32] have been successfully fabricated by high vacuum deposition using elemental precursors on the basis of solid state reactions. According to Kim *et al.*[29] and Mavrokefalos *et al.*'s studies[32] respectively, in the first example, Te nanoparticle-dispersed $Bi_{0.5}Sb_{1.5}Te_3$, in which the amount of ~15 nm diameter Te nanoparticles is increased up to 15 vol. %, the Seebeck value is significantly improved from 169 to 248 μV/K with a moderately reduced electrical conductivity, thus resulting in an enhanced zT value by more than 30% due to the hot carrier filtering effect as predicted by Faleev's calculation.[24] In a second example, the in-plane thermal

conductivity is measured to be three times lower in misfit-layered $[(PbSe)_{0.99}]_m(WSe_2)_n$ superlattice thin films than in disordered-layered WSe_2 because of interface scattering.

1.3.3 Drawbacks and challenges in hetero-structure fabrication

While it is valuable to investigate the physical properties of the atomically defined, highly crystallized thin films that are fabricated as hetero-structures by high vacuum deposition procedures, up-scaled syntheses of materials with designed structures are highly desirable, especially for thermoelectric applications. We will a variety of hetero-structures synthesized by either mechanical mixing techniques or solution based chemical syntheses. In contrast to the thin film hetero-structures for which the physics and thermoelectric properties have been extensively studied, the synthesis and modeling of bulk, poly-crystallize, and multi length scaled material systems are formidable. Impurities and interfacial boundaries induced by bulk-scaled synthetic routes are for the most part inevitable. The key challenge for the materials chemist is the development of controllable and straightforward synthetic methodologies that will integrate multiple phases with scalar designed physical properties. The intent of this review is to give a brief summary of some of the current bulk scaled approaches that might help guide researchers design optimal hetero-structures for further improvement of thermoelectric conversion efficiency.

2. Bulk scaled approaches to inhomogeneous hetero-structures

In the development of hetero-structures with enhanced thermoelectric performance, the use of inhomogeneous precursor nanophase mixtures in the early synthesis stages is a valuable approach because of its simplicity. This strategy has been applied to a variety of material systems including telluride, half-Heusler and skutterudite.[33-36] For example, Zhang *et al.* and Sumithra *et al.* reported a simple methodology to obtain micro-nano hetero-structures by mixing the metallic nanoparticles (Ni_2Te and Bi) and semiconducting micrometer scaled particles as shown in **Figure 6(a)**.[33,34] In addition, for the half-Heusler material system, Birkel *et al.* used a solid-state reaction to form full-Heusler compounds in a half-Heusler matrix by adding small amount of excess Ni to the starting reactants as shown in Figure 6(b).[35]

One of the common characteristics in these three reported hetero-structures is the use of inhomogeneous metallic microstructures, which limits the extent of metal-semiconductor interfaces. In addition, a change in the charge carrier densities resulting from the impurities suppresses an improvement of the power factors. Therefore, in contrast to the prediction of Faleev *et al.*'s model,[24] the power factors of these inhomogeneous hetero-structures do not exhibit a significant improvement. However, compared to the metallic inclusion free semiconductor, these hetero-structures process a somewhat lower thermal conductivity, which is mainly due to the irregular microstructure induced phonon scattering. According to a systematic study by Zhao *et al.* on the length scale of grains,[37] this extent of reduction in lattice thermal conductivity using metallic inclusions incorporated to make the hetero-structure is similar to that for the single phase semiconductors made with approximately the same amount of nanoscaled particles. This means that from a synthetic prospective, increasing the power factor is more difficult to accomplish than reducing the thermal conductivity. The inhomogeneous hetero-structures made by straightforward routes in general are not able to create the desired interfacial barriers and/or band bending that is necessary to selectively scatter the carriers as predicted by theoretical models, but are able to scatter the long-wavelength phonons as a result of the existence of their irregular microstructure characteristics. However, it is important to note that this extent of reduction is not strong (~ 20-30%), even with a relatively large number of nanoscaled/micron-sized inclusions, which suggests that the inhomogeneously dispersed microstructures are not as efficient as homogenous nanostructures in terms of phonon scattering. It is clear that the further development of synthetic methodologies that give a homogeneous dispersion of the minor phase into the bulk matrix of a hetero-structure is highly desirable, as discussed in section 3 below.

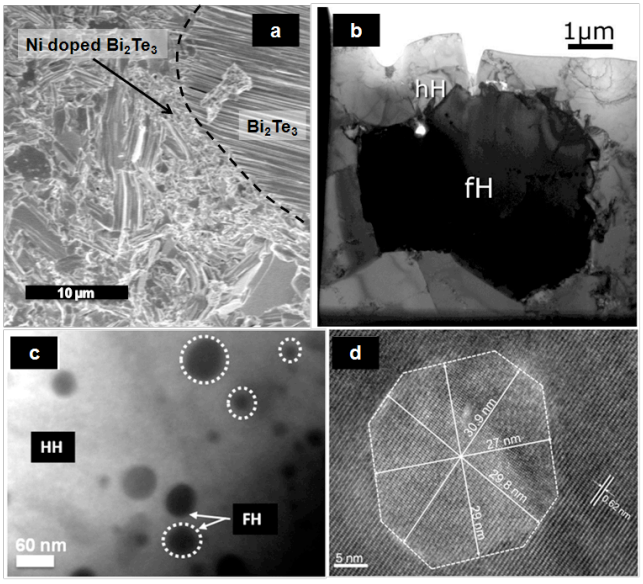

Figure 6. (a) The cross-sectional microscopic image of Ni_2Te doped Bi_2Te_3 hetero-structures. The labels indicates the inhomogeneous dispersion of stoichiometric Bi_2Te_3 and Ni doped inclusions. (b) the transmission microscopic image of the inhomogeneous composite of half-Heusler (hH) and full-Heusler (fH). (c), (d) Low (c) and high (d) magnification image of the nanocomposite with x = 0.04 showing fH nanoparticles with broad size distribution (10–60 nm) coherently embedded inside the hH ($Ti_{0.1}Zr_{0.9}NiSn$) matrix. No noticeable strain is observed at the interface between the

particle and the matrix, suggesting endotaxial insertion with minimal lattice distortion of the fH particle within the hH matrix. Parts a, c, d reprinted with permission from refs. 33, 41. Copyright 2010, 2013 American Chemical Society. Part b reproduced from ref. 35 with permission from the PCCP Owner Societies.

3. Bulk scaled approaches to homogeneous hetero-structures

Both solid-state syntheses and solution based chemistry strategies have been reported for homogeneous hetero-structures.[38–53] Solid-state syntheses usually produce material systems with higher zT values than does solution based chemistry, mainly because a high temperature process above the melting point can be used to minimize or better define impurity composition and distribution.[54] However, this process is limited to phase combinations that are thermodynamically favored at high temperature. Moreover, the dispersion of the nanometer scaled domains requires careful control of the phase immiscibility which is not universal for all the phase combinations that are of interest. For example, for the preparation of a metallic full-Heusler minor phase in a half-Heusler semiconductor major phase, as for $TiNi_{1+x}Sn$, the microwave synthesis plus spark plasma sintering procedures reported by Birkel *et al.* results in an inhomogeneous dispersion of the metallic full-Heusler compound in the semiconducting half-Heusler matrix.[35] In contrast, for $(Zr,Ti)Ni_{1+x}Sn$, made by conventional melting plus hot pressing procedures, the metallic full-Heusler inclusions are more homogeneous at the nanoscale as shown in Figure 6(c) and (d).[41] These contradictory observations drawn from two similar material systems show, not unexpectedly, that the processing conditions can greatly modify the resulting hetero-structure properties.. In this review, the two main methodologies, solid-state reaction and solution based routes, are discussed further in section 3.1 and 3.2, respectively.

3.1 Solid-state syntheses of homogeneous hetero-structures

Although bulk scaled homogeneous hetero-structures produced by solid-state syntheses have similar structures, because of the differences in the intrinsic properties and band structures of the minor phase and major matrix, no unanimous conclusion on the effects of those nano-inclusions can be drawn except for the reduction in lattice thermal conductivity.[41–49] **Figure 7** summarizes the structures currently reported including PbS,[44] SrS,[45] CdS,[46] SrTe,[47] CdTe[48] and Ag_2Te[49] in the PbTe or PbS matrix. Particularly in the cases of SrS-PbS[45] and SrTe-PbTe,[47] the strain maps in **Figure 8** show considerable elastic strain at and around all nanoscaled precipitates. This is mainly due to the formation of coherent or semi-coherent boundaries at the nanoscale (<10 nm).

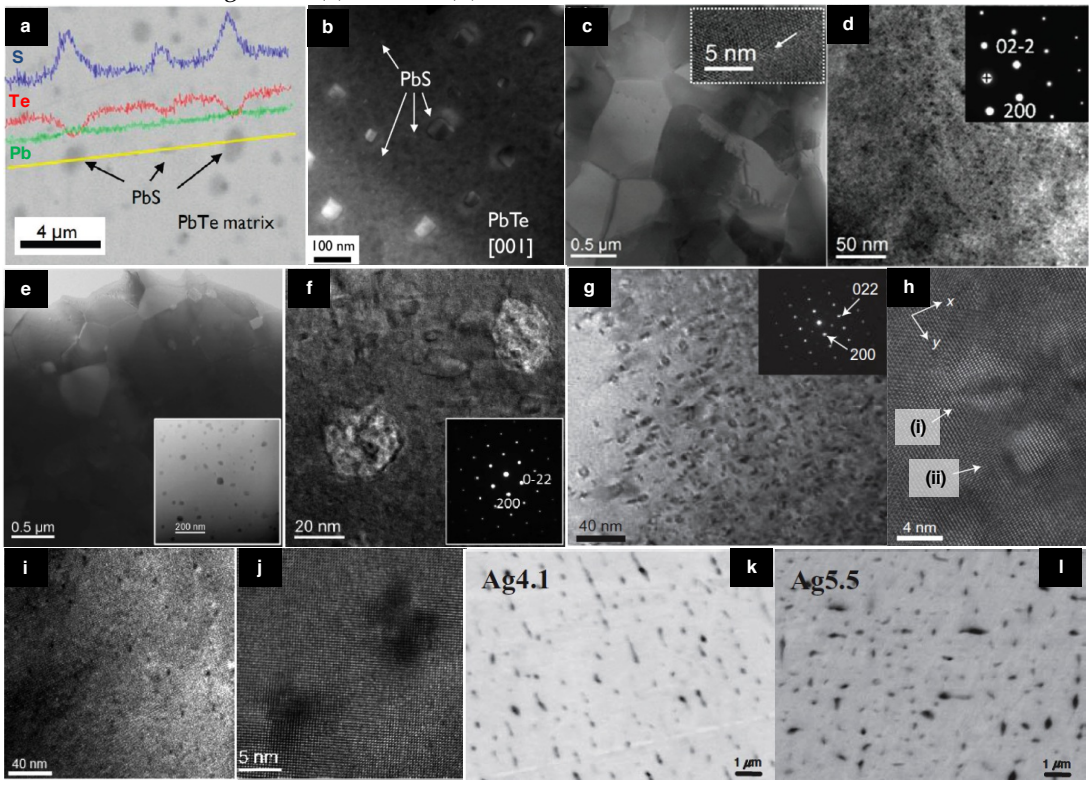

Figure 7. Microscopic images of the hetero-structures: (a), (b) 8% PbS-PbTe; (c), (d) 3% SrS-PbS; (e), (f) 3% CdS-PbS; (g), (h) 2% SrTe-PbTe; (i), (j) 1% CdTe-PbTe; (k) 4.1% Ag_2Te-PbTe; (l) 5.5% Ag_2Te-PbTe. Here, "A-B" represents "A" inclusions embedded in

"B" matrix. Specifically, (a) is the EDS line scans that reveal the darker PbS particles show increased counts for S and decreased Te. The inset in (c) is the high-resolution TEM image of one grain boundary and that in (d) is the corresponding diffraction pattern along [011] direction shows all spots from PbS matrix. The inset in (e) is the STEM image shows high number density nanostructures and that in (f) is the corresponding diffraction pattern along the [011] direction. The inset in (g) is the corresponding diffraction pattern, which confirms the crystallographic alignment of SrTe and PbTe lattices. Reproduced with permission from refs. 44 - 49. Copyright 2010, 2012 American Chemical Society, 2011 Nature Publishing Group, and 2011 Wiley-VCH Verlag.

According to the work done by He *et al.*, these nanoscaled structures with the correlated dislocations and the resultant strains have been confirmed to produce materials with more efficient reductions in thermal conductivity at high temperature.[50] With respect to improving the electronic properties, especially the Seebeck coefficient, no dramatic improvement has been reported, for several possible reasons: (1) the band offsets between two semiconducting phases (PbS and CdS or ZnS) are rather small (< 0.13 eV at 0 K), and accordingly play only a minor role in producing hot carrier filtering;[44,46] (2) the inclusions are strong dopants, which compensate for the intrinsic carriers, resulting in an extraordinarily large change in carrier density. For example, Cu-based inclusions in p-Bi_2Te_3 switch the conductivity type from p to n as the mole concentration of Cu goes from 0% to 5%.[43] However, there are still a few interesting observations about the Seebeck coefficient enhancement without losing the electrical conductivity. For example, in the layered oxide system ($Ca_3Co_4O_{9+\delta}$)[42] and the half-Heusler system,[41] the metallic inclusions are shown to increase the Seebeck coefficient significantly as a result of the hot carrier filtering effect due to the appropriate band alignment among multiple phases. (**Figure 9**)

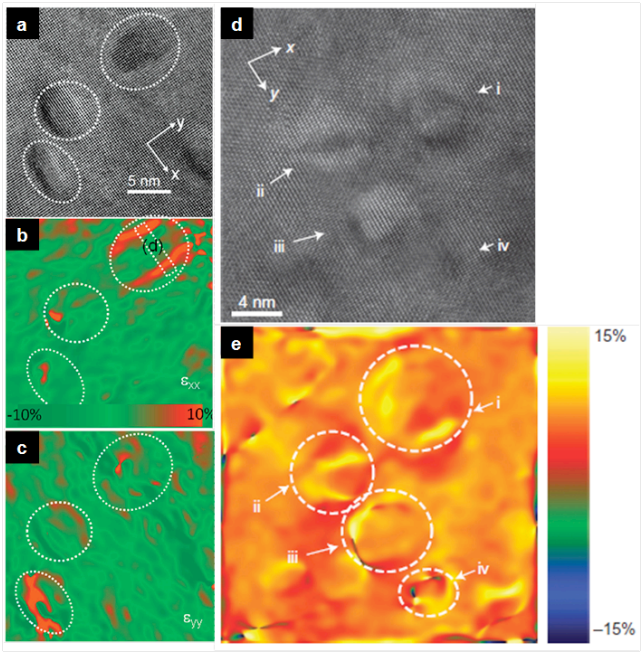

Figure 8. (a)-(c), high magnification TEM image (a) and ε_{xx} (b), ε_{yy} (c) strain maps of the image (a) of $Pb_{0.975}Na_{0.025}S$ with 3% SrS sample. (d), (e) high magnification TEM image (d) and shear strain distribution map of the image (d) of 2% SrTe in PbTe. Reproduced with permission from ref. 45 and ref. 47. Copyright 2012 American Chemical Society and 2011 Nature Publishing Group.

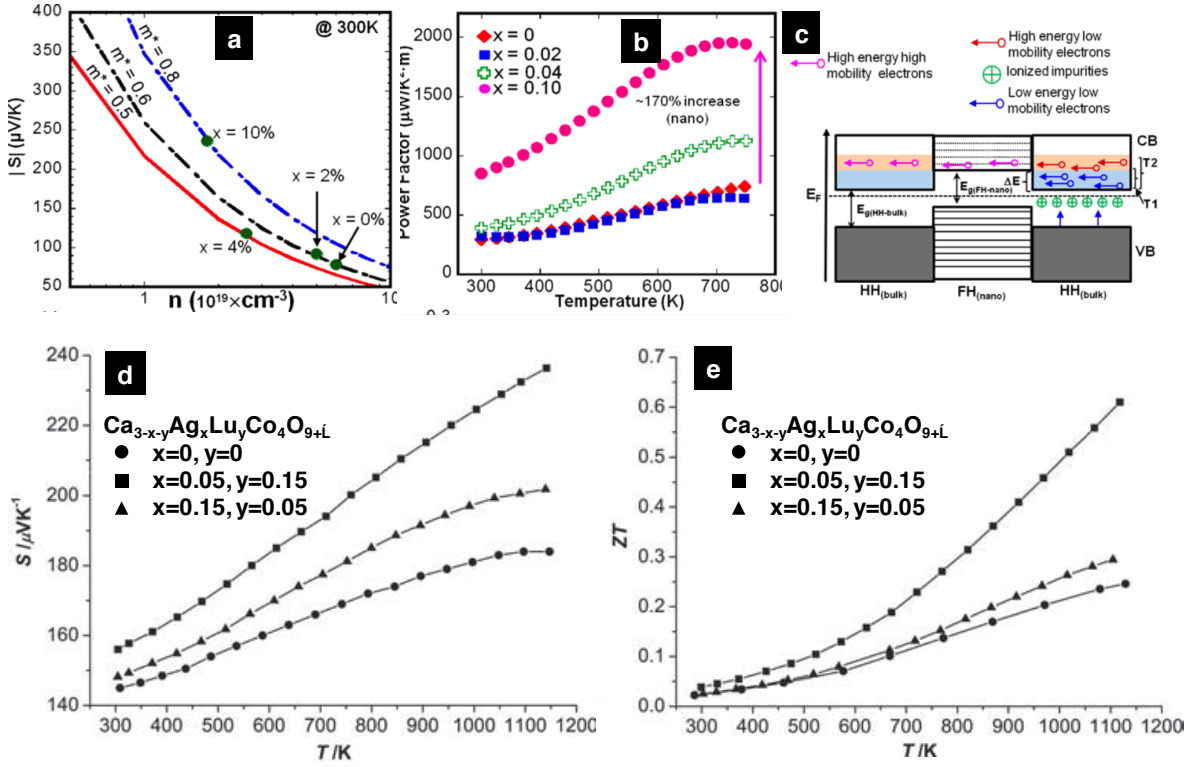

Figure 9. (a) Pisarenko plot of $Ti_{0.1}Zr_{0.9}Ni_{1+x}Sn$ nanocomposites, which shows large enhancements of the thermopower (S) due to simultaneous decrease in carrier concentration and increase in the carrier effective mass (m*) with increasing excess Ni. (b) Temperature-dependent thermoelectric figure of merit (zT) of hH(1–x)/fH(x) bulk nanocomposites (x=0, 0.02, 0.04, and 0.1). (c) Proposed mechanism of the filtering of low energy electrons (from CB of hH) at the potential barrier, ΔE, (reducing effective carrier density) and spatial separation of high-energy electrons (within CB of fH) from ionized-impurities at nanometer scale hH/fH heterojunctions. Cyan and orange colors represent distributions of low-energy and high-energy electrons at temperatures T1 and T2 (T2 > T1) within the CB of the HH matrix. (d), (e) Temperature dependence of (d) Seebeck coefficient (S) and (e) dimensionless figure of merit for $Ca_{3-x-y}Ag_xLu_yCo_4O_{9+\delta}$ with x,y = 0, x=0.05, y=0.15, and x=0.15, y = 0.05. Reprinted with permission from ref. 41 and ref. 42. Copyright 2013 American Chemical Society and 2011 Wiley-VCH Verlag.

3.2 Solution-grown hetero-structures

The preparation of hetero-structures with second phase inclusions introduced by solid-state syntheses usually parallels the top-down synthesis strategy. In contrast, the bottom-up approaches aim to create the products from molecular precursors *via* a low-temperature chemical reaction. Some of the nanostructures grown are shown in **Figure 10**.[51–53] For example, Yin and co-workers produced Bi_2Te_3-Te heterogeneous nanostructures that are composed of Bi_2Te_3 nanoplates and Te nanorods with various morphologies ("nails", "barbells", "syringes", and "accordions") by controlling the reduction kinetics of TeO_3^{2-} and Bi^{3+} respectively.[51] However, according to the studies done by Ramanath and co-workers,[52] p-type Te in n-type Bi_2Te_3 is not ideal for thermoelectric application since both types of carriers will cancel the thermoelectric effect to produce a lower Seebeck coefficient. Instead, p-Sb_2Te_3 and Te phase combinations may increase the Seebeck value significantly, by two- to three-fold.

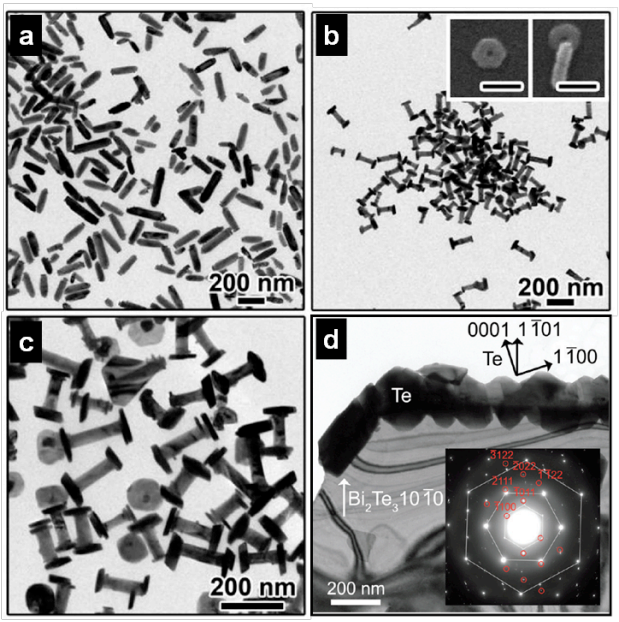

Figure 10. TEM images of the Bi_2Te_3-Te hetero-structures. (a)-(c) the products prepared by Wang *et al.*[51] using different amounts of diluted hydrazine (2 M) in the presence of 15 μL of $FeCl_3$/EG stock solution: (a) 130, (b) 140, and (c) 150 μL. The insets in (b) are SEM images of a broken barbell structure. The scale bars in the insets are 100 nm. (d) the product prepared by Mehta *et al.*[52] using microwave synthesis under tri-*n*-octylphosphine (TOP) protection. The inset is the corresponding [0001] zone diffraction pattern exhibiting Bragg reflections from Bi_2Te_3 (hexagonal spot pattern) and Te (red circles). Reprinted with permission from ref. 51 and ref. 52. Copyright 2010 American Chemical Society.

Although encouraging in terms of Seebeck enhancement, the overall zT values of solution-synthesized nanostructures have been rarely reported, and more effort on this aspect is needed. Especially noteworthy is the example of PbTe-PbS hetero-structures made by the solution syntheses[53] analogous to the structures made by solid-state syntheses in ref. 44 as discussed above. As shown in **Figure 11(a)**, the hetero-structured composite is built on the building blocks of core-shell nanoparticles. By controlling the relative dimensions between the core and shell, the concentration of the inclusions can be tuned. Figure 11(b) confirms the well-defined core-shell structure of the nanoparticles. After annealing, this composite with two semiconducting phases (PbS and PbTe) exhibits a comparable extent of reduction in thermal conductivity as that in ref. 44, and thereby has a high zT of over 1.0 at ~ 700 K, which is slightly lower (~ 20%) than the zT record for the same compositions, but made by solid-state syntheses. This result shows considerable promise for the use of solution syntheses to generate high zT values, and thus avoid high temperature processes. This offers opportunities both for thermoelectric design and for the reduction of bulk fabrication costs.

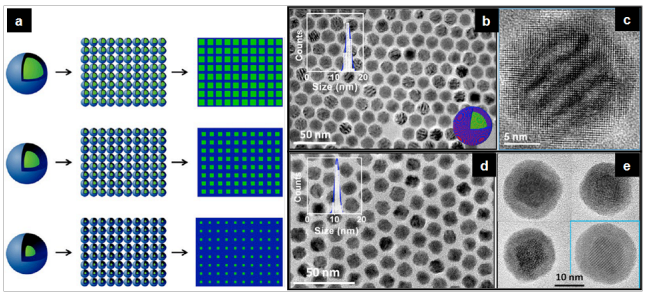

Figure 11. (a) Steps for the production of nanocomposites from the bottom-up assembly of core-shell nanoparticles with different shell thickness. (b), (c) TEM images of $(PbTe)_{0.28}$@$(PbS)_{0.72}$ core-shell nanoparticles with crystalline PbS shells. (d), (e) TEM images of $(PbTe)_{0.25}$@$(PbS)_{0.75}$ core-shell nanoparticles having amorphous PbS shells. Insets display the histogram of the particle size distribution. Adapted with permission from ref. 53. Copyright 2013 American Chemical Society.

The three examples discussed above summarize the current state-of-the-art for solution-grown hetero-structures. From the prospective of energy-conversion efficiency, all the reports to date offer opportunities for significant improvement in the future. However, these examples give alternatives for the assembly of phase combinations and nanostructures that are difficult to produce by ordinary solid-state synthesis techniques.

3.3 Solution-based assembly of hetero-structures

Unlike the materials discussed in section 3.2, in this category, solution-based chemistry is used to assemble multiple phases together homogeneously to form a hetero-structured system. This idea was first inspired by the pioneering work done by Murray and co-workers in 2004.[55] In their early studies, two types of nanocrystals, PbTe and Ag_2Te, were assembled together by controlling the surface chemistry. The drawback of this route is low electronic mobility, which limits its application for thermoelectric applications. Also in 2004, hydrazine-based zintl ion chemistry was reported by Mitzi *et al.*,[56] and this has since played an important role in the development of bulk scaled approaches for the synthesis of conducting materials. In the first example of $[Sn_2S_6]^{4-}$,[56] the SnS_2 compound plus excess sulfur was shown to be soluble in pure hydrazine to form a clear solution. One of the most important features of this precursor is the ease of conversion from solution phase to solid state, conducting phase *via* solvent evaporation and annealing.

Besides $[Sn_2S_6]^{4-}$, other metal chalcogenide compounds such as ZnTe,[57] GeSbSe,[58] CuS,[59] and CuInSe[60] have been developed using a similar strategy. In 2009, these molecular metal chalcogenides (MMC), for example, $[Sn_2S_6]^{4-}$, were demonstrated to successfully exchange with the organic capping ligand used in the synthesis of the metal nanoparticles.[61] After the exchange, the metal nanoparticles are suspended in the hydrophilic phase (hydrazinium precursor) while the organic surfactants are

left in the hydrophobic layer (organic non-polar solvent). After spin-coating the exchanged metal nanoparticles on substrate, the nanoparticles assemble together with an "inorganic" capping ligand. After annealing, the "inorganic" capping ligand crystallizes to form an inorganic solid-state inter-layer to facilitate electron transport in plane as shown in **Figure 12**.

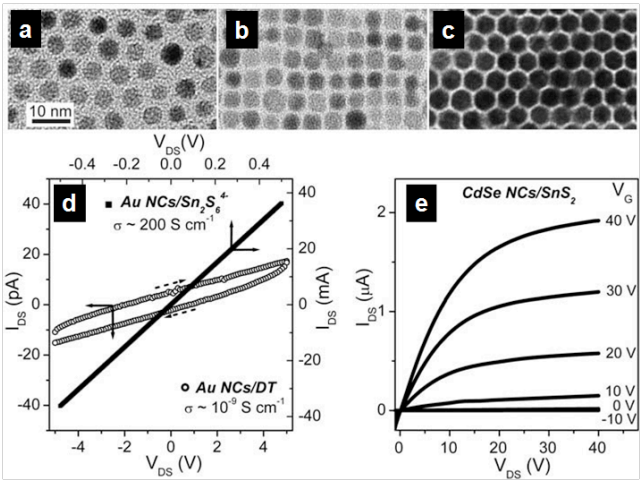

Figure 12. (a) TEM image of an array of ~5-nm Au NCs capped with dodecanethiol. (b) TEM image of a layer of ~5-nm Au NCs capped with $(N_2H_5)_4Sn_2S_6$. (c) TEM image of a three-dimensional superlattice of ~5-nm Au nanocrystals capped with $(N_2H_5)_4Sn_2S_6$. (d) Current-voltage (I-V) scans for a film of dodecanethiol-capped 5-nm Au nanocrystals (open circles) and for a film of the same Au NCs capped with $(N_2H_5)_4Sn_2S_6$ (black squares). Dashed arrows show the voltage scan direction. (e) Plot of drain current ID versus drain-source voltage V_{DS} for a nanocrystal FET with a channel composed of 4.5-nm CdSe nanocrystals capped with $(N_2H_5)_4Sn_2S_6$ and annealed at 200°C (channel length 10 mm, width 3800 mm, 110-nm-thick SiO_2 gate dielectric). From ref. 61. Reprinted with permission from AAAS.

Based on these studies, the Stucky and Murray groups have recently reported hetero-structured bulk-scale thick films of Ag@Sb_2Te_3-Te[62] and Pt@Sb_2Te_3[63]. In their reports, the hydrazinium precursor that comprises antimony telluride and excess tellurium is used to exchange the organic surfactants that cap the Ag or Pt nanoparticles and thereby form a homogeneous dispersion of metallic nanophases. After solvent evaporation and annealing, the molecular metal chalcogenide crystallizes to form a semiconducting matrix with Ag or Pt incorporated metallic nano-inclusions. The interfacial band bending formed corresponds to a Schottky contact for Ag-Sb_2Te_3/Te and an Ohmic contact for Pt-Sb_2Te_3 respectively. Interestingly, the relative improvement in zT values of both samples is the same (see **Table 1**), although the preparation conditions are slightly different. It is worth noting that the carrier densities may increase once the metallic nano-inclusions are introduced; however, in a comparison to the nano-inclusion-free semiconductor, the hetero-structure exhibits a higher Seebeck coefficient at higher carrier density, which strongly suggests a hot electron improvement of Seebeck coefficient. This is in agreement with Faleev *et al.*'s prediction;[24] both types of band bending (Figure 3(b) and (c)) are able to significantly improve the Seebeck coefficient.

In contrast to the high work-function noble metal inclusions like Pt, in the study of Ag-based inclusions, researchers found that the high solubility of Ag in Te limited the annealing and operating temperature.[62] Because Ag@Sb_2Te_3 is less thermally stable than Pt@Sb_2Te_3, a metal oxide coating of the metallic Ag nanoparticles is necessary in order to reduce the diffusion of Ag into the surrounding semiconducting telluride media. Recently, the Stucky group developed a route to grow a thin layer of oxide (~3 nm) to protect the Ag nanoparticles by atomic layer deposition (ALD).[64] The enhancement of the Seebeck coefficient is predicted by a computer simulation by Shakouri, Stucky, and co-workers that includes an extensive ionized impurity scattering mechanism as well as a cut-off potential of 0.2 eV for hot carrier filtering.[64]

This is the first demonstration of hot electron filtering with both experimental and theoretical evidence for solution processed thermoelectric hetero-structures. The enhancement of thermoelectric Seebeck and conductivity results in an improvement of the zT value by a factor of two to ~1.0 at 460 K. This is an exceptionally high value compared to other single-phase semiconductors processed in solution with similar composition and carrier density.

4. Other hybrid hetero-structures

4.1 Carbon nanotube (CNT)-based hybrid structures

Recently, studies of the thermoelectric properties of carbon-based nanomaterials such as carbon nanotubes (CNTs) and graphenes have attracted more and more attention. Kim and co-workers investigated the thermoelectric power of individual single-walled carbon nanotubes (SWNTs) and discovered that the measured thermoelectric power correlated well with the electrical conductance across the SWNT according to the Mott formula (E3).[65] However, due to the metallic nature of the SWNTs with the expected inherently high thermal conductivity and low Seebeck coefficient, the composite made solely by CNTs does not provide a respectable thermoelectric efficiency.[66–68] Consequently, extensive effort in this field

Table 1. Thermoelectric properties at room temperature and compositions of the hetero-structures and the control samples in refs. 62 and 63.

Reference Number	Composition	Carrier Density cm^{-3}	Mobility $cm^2 \cdot V^{-1} \cdot s^{-1}$	Seebeck Coefficient μV/K	Conductivity $S \cdot cm^{-1}$	Power Factor $\mu W/(cm \cdot K^2)$
62	$Ag@Sb_2Te_3$-Te	8.9×10^{19}	4.1	+135	56	1.02
63	$Pt@Sb_2Te_3$	2.5×10^{19}	11	+152	27	1.02
62	Sb_2Te_3	1.7×10^{19}	26	+114	70	0.91
63	Sb_2Te_3	1.7×10^{19}	28	+116	73	0.96

has focused on hybrid composites in which the CNTs act as additives. These hybrid structures include structural polymer-CNTs,[69–77] conductive polymer-CNTs,[78–81] metal decorated CNTs[82–84] and solid-state compound-CNTs.[85–87] The main function of CNTs in the polymer is to facilitate the electron transport by creating electron transport pathways and retain the low thermal conductivity as illustrated in **Figure 13**.

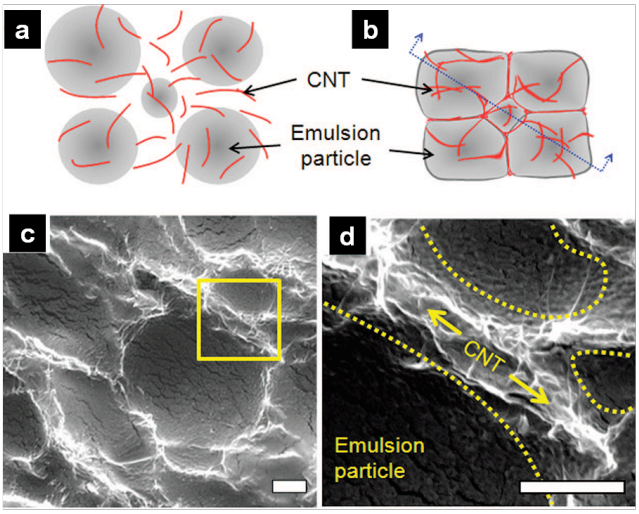

Figure 13. (a) Schematic of CNTs suspended in an aqueous emulsion. Gray spheres and red lines represent emulsion particles and CNTs, respectively. (b) Schematic of the emulsion-based composite after drying. The CNTs form a three-dimensional network along the surfaces of the spherical emulsion particles. (c), (d) SEMs of the cross-sections of 5 wt. % CNT in poly(vinyl acetate) (PVAc). The high-magnification SEM shown in (d) is a portion of the sample in (c) indicated by a yellow solid square. It clearly shows that CNTs (indicated by arrows) are wrapped around the emulsion particles (indicated by yellow dotted lines). The scale bars in the SEMs indicate 1 μm. Reprinted with permission from ref. 69. Copyright 2008 American Chemical Society.

Substantial progress in understanding and predictively designing the properties of carbon nanotube (CNT)-based hybrid structures is being made. For example, a zT value of 1.2 has been reported for a hybrid system made using a solid-state semiconductor and CNTs. As demonstrated by Zhang and co-workers, a ~20% relative improvement in zT is obtained for hybrid Bi_2Te_3-CNTs over the CNT-free sample.[87] However, the mechanism of this synergistic effect has yet to be resolved. This can be contrasted with the power factor of 160 $\mu W/(m \cdot K^2)$ that is achieved for the carbon based composite made up of SWNTs, poly(3,4-ethylenedioxythiophene): poly(styrenesulfonate) (PEDOT:PSS) and polyvinyl acetate (PVAc).[81] The overall zT values reported (10^{-3} to 10^{-2}) for this organic materials are approximately two orders of magnitude lower than those observed for typical solid-state semiconductors.

4.2 Conductive polymer based organic-inorganic hybrid structures

The use of conductive polymers for thermoelectric application was inspired by the thermoelectric measurement of single molecules such as thiol- and isocyanide-terminated aromatic molecules.[88] An important breakthrough in this field was reported by Crispin and co-workers,[89] in which the zT of poly(3,4-ethylenedioxythiophene) (PEDOT) approached 0.25 at room temperature by controlling the oxidation level of PEDOT.

As for CNTs, it is possible to combine the relatively efficient conductive polymers with inorganic semiconductors to form a hybrid inorganic-organic system such as Te-PEDOT:PSS[90] and poly(3-hexylthiophene) (P3HT)-Bi_2Te_3.[91] In the former example, the zT value is ~0.1, more than two orders of magnitude higher than bare Te and PEDOT:PSS, as a result of the greatly higher conductivity and the respectable Seebeck coefficient shown in **Table 2**. In the latter system, the authors depicted the possible band alignment between p-type Bi_2Te_3 and organic P3HT. One advantage of incorporating the organic phase is the ease of band tuning by changing the doping level. For example, in the 24 wt.% doped P3HT system, the band gap of P3HT is 0.2 eV, which forms a potential barrier at the P3HT-Bi_2Te_3 interface below 0.1 eV, and therefore selectively scatters low-energy carriers rather than high-energy carriers. As a consequence, the Seebeck coefficient of the hybrid is 118 μV/K, almost five times higher than that of the bare P3HT (24 μV/K).[91] In summary, although these hybrid systems do not exhibit zT values as high as other solid-state hetero-structures, great progress is being made. It is expected that the highly accessible tunability of each of the components will facilitate maximization of the overall power efficiency and zT.

5. Summary and Outlook

As illustrated in **Figure 14**, hetero-structures have proven to be an enabling route to the improvement of zT in comparison with the zT values for single-phase nanostructures. In Figure 14, different hetero-structures are categorized into several groups based on their base

semiconductors (polymers, Bi_2Te_3, lead chalcogenide and oxide). Generally, the hetero-structures prepared by solid-state syntheses (column) exhibit higher zT values than those from the materials made by solution assembly or syntheses (cubic). But the low-temperature solution-processed hetero-structures are catching up with zT values that are over 1.0.

Table 2. Room temperature thermoelectric properties of Te/PEDOT:PSS nanocomposites and control films. Adapted with permission from ref. 90. Copyright 2010 American Chemical Society.

System	σ (S/cm)	S (μV/K)	Power Factor (μW/(m·K²))	κ (W/(m·K))	zT_{max}
Hybrid	19.3 (±2.3)	163 (±4)	70.9	0.22-0.30[a]	0.10
PEDOT:PSS	1.32 (±0.12)	18.9 (±0.2)	0.05	0.24-0.29	6×10^{-5}
Te nanowires	0.08 (±0.03)	408 (±69)	2.7	2[b]	4×10^{-4}

[a] Films prepared in identical manner to those used for electrical measurements. [b] Bulk value.[92] Reported errors are standard deviations.

Although the mechanisms of phonon/electron transport in a variety of hetero-structures with different compositions and microstructures are not identical or unambiguous, several conclusions can be drawn based on current literature results: (1) homogeneous dispersion of a minor phase into the major-phase matrix is more efficient for both phonon scattering and hot carrier filtering than is an inhomogeneous dispersion; (2) hot carrier filtering requires an appropriate interfacial barrier or band bending to selectively scatter low-energy carriers; (3) the barrier height must be below 0.2 eV for selective scattering and in order to maintain or enhance carrier mobility; (4) the combination of multiple phases must be thermally stable. In other words, the insolubility of one phase into the other must remain constant over the entire temperature range of processing and operations.

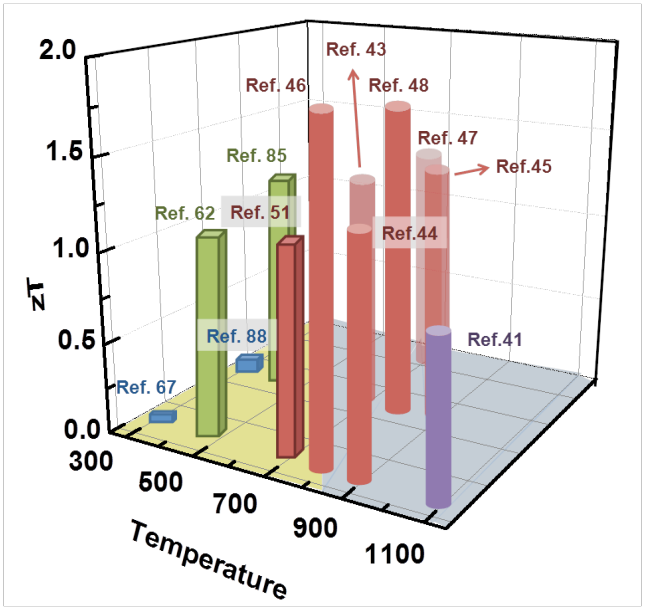

Figure 14. Summary of zT values of the bulk scaled hetero-structures discussed in this review. CNTs, Bi_2Te_3, PbTe and oxide based hetero-structures are shown in blue, green, red and purple respectively. The cube on yellow base indicates the corresponding synthetic route is solution based and the column on blue base indicates the route is solid-state based. The corresponding reference is labeled respectively.

Chemistry synthesis techniques are a double-edged sword. Impurity levels are inherently higher than they are for MBE or clean room synthetic procedures, so that there are more synthetic variables to control in terms of composition, hierarchical structure and property scaled hetero-structure assembly. This larger synthesis phase space in principle can be valuable for providing access for the enabling of complex composite thermoelectric materials with high power efficiencies. We believe that to do this with bulk synthesis chemistry techniques, high throughput screening is highly desirable. The optimal phase combination has to be selected from a comprehensive library of hetero-structures. For example, in addition to Ag@Sb_2Te_3-Te[62] and Pt@Sb_2Te_3,[63] screening of numerous other types and combinations of metals is needed. In addition, compared to the solid-state-synthesized hetero-structures, low-temperature processes based on hydrazinium chemistry or polymer chemistry offer some flexibility of time and processing for the fabrication of thermoelectric devices.[89]

ACKNOWLEDGMENT

The authors are grateful for support from the Center for Energy Efficient Materials, an Energy Frontier Research Center funded by the U.S. Department of Energy, Office of Science, Basic Energy Sciences under Award DE-SC0001009.

REFERENCES

(1) Toberer, E. S.; May, A. F.; Snyder, G. J. *Chemistry of Materials* **2010**, *22*, 624–634.

(2) Snyder, G. J.; Toberer, E. S. *Nature Materials* **2008**, *7*, 105–14.

(3) Seebeck, T. J.; Oettingen, A. v. Magnetische Polarisation der Metalle und Erze durch Temperatur-Differenz, Leipzig, W. Engelmann, **1895**; pp. 265–373. http://catalog.hathitrust.org/api/volumes/oclc/7502427.html

(4) Peltier, J. C. *Annales de Chimie* **1834**, *56*, 371-386.
(5) Poudel, B.; Hao, Q.; Ma, Y.; Lan, Y.; Minnich, A.; Yu, B.; Yan, X.; Wang, D.; Muto, A.; Vashaee, D.; Chen, X.; Liu, J.; Dresselhaus, M. S.; Chen, G.; Ren, Z. *Science* **2008**, *320*, 634–638.
(6) Joshi, G.; Lee, H.; Lan, Y.; Wang, X.; Zhu, G.; Wang, D.; Gould, R. W.; Cuff, D. C.; Tang, M. Y.; Dresselhaus, M. S.; Chen, G.; Ren, Z. *Nano Letters* **2008**, *8*, 4670–4674.
(7) Yan, X.; Poudel, B.; Ma, Y.; Liu, W. S.; Joshi, G.; Wang, H.; Lan, Y.; Wang, D.; Chen, G.; Ren, Z. F. *Nano Letters* **2010**, *10*, 3373–3378.
(8) Xie, W.; He, J.; Kang, H. J.; Tang, X.; Zhu, S.; Laver, M.; Wang, S.; Copley, J. R. D.; Brown, C. M.; Zhang, Q.; Tritt, T. M. *Nano Letters* **2010**, *10*, 3283–3289.
(9) Mehta, R. J.; Zhang, Y.; Karthik, C.; Singh, B.; Siegel, R. W.; Borca-Tasciuc, T.; Ramanath, G. *Nature Materials* **2012**, *11*, 233–40.
(10) Kovalenko, M. V; Spokoyny, B.; Lee, J.; Scheele, M.; Weber, A.; Perera, S.; Landry, D.; Talapin, D. V. *Journal of the American Chemical Society* **2009**, *131*, 597–602.
(11) Dirmyer, M. R.; Martin, J.; Nolas, G. S.; Sen, A.; Badding, J. V. *Small* **2009**, *5*, 933–7.
(12) Scheele, M.; Oeschler, N.; Meier, K.; Kornowski, A.; Klinke, C.; Weller, H. *Advanced Functional Materials* **2009**, *19*, 3476–3483.
(13) Tang, J.; Wang, H.-T.; Lee, D. H.; Fardy, M.; Huo, Z.; Russell, T. P.; Yang, P. *Nano Letters* **2010**, *10*, 4279–4283.
(14) Zhang, Y.; Day, T.; Snedaker, M. L.; Wang, H.; Krämer, S.; Birkel, C. S.; Ji, X.; Liu, D.; Snyder, G. J.; Stucky, G. D. *Advanced Materials* **2012**, *24*, 5065–5670.
(15) Toberer, E. S.; Baranowski, L. L.; Dames, C. *Annual Review of Materials Research* **2012**, *42*, 179–209.
(16) Dames, C.; Chen, G. In *ThermoelectricsHandbook: Macro to Nano*; Rowe, D. M., Ed.; CRC Press: Boca Raton, FL; p. 1014.
(17) Li, D. Y.; Wu, Y. Y.; Kim, P.; Shi, L.; Yang, P. D.; Majumdar, A. *Applied Physics Letters* **2003**, *83*, 2934–36.
(18) Biswas, K.; He, J.; Blum, I. D.; Wu, C.-I.; Hogan, T. P.; Seidman, D. N.; Dravid, V. P.; Kanatzidis, M. G. *Nature* **2012**, *489*, 414–418.
(19) Chiritescu, C.; Cahill, D. G.; Nguyen, N.; Johnson, D.; Bodapati, A.; Kebilinski, P.; Zschack, P. *Science* **2007**, *315*, 351-353
(20) Cahill, D. G.; Watson, S. K.; Pohl, R. O. *Physical Review B* **1992**, *46*, 6131–6140.
(21) Popescu, A.; Woods, L.; Martin, J.; Nolas, G. *Physical Review B* **2009**, *79*, 205302.
(22) Zhou, J.; Li, X.; Chen, G.; Yang, R. *Physical Review B* **2010**, *82*, 115308.
(23) Moyzhes, B.; Nemchinsky, V. *Applied Physics Letters* **1998**, *73*, 1895–1897.
(24) Faleev, S.; Léonard, F. *Physical Review B* **2008**, *77*, 214304.
(25) Heremans, J.; Thrush, C.; Morelli, D. *Physical Review B* **2004**, *70*, 115334.
(26) Vashaee, D.; Shakouri, A. *Physical Review Letters* **2004**, *92*, 106103.
(27) Zebarjadi, M.; Esfarjani, K.; Shakouri, A.; Bahk, J.-H.; Bian, Z.; Zeng, G.; Bowers, J.; Lu, H.; Zide, J.; Gossard, A. *Applied Physics Letters* **2009**, *94*, 202105.
(28) Zide, J.; Vashaee, D.; Bian, Z.; Zeng, G.; Bowers, J.; Shakouri, A.; Gossard, A. *Physical Review B* **2006**, *74*, 205335.
(29) Kim, S. Il; Ahn, K.; Yeon, D.-H.; Hwang, S.; Kim, H.-S.; Lee, S. M.; Lee, K. H. *Applied Physics Express* **2011**, *4*, 091801.
(30) Kim, S. I.; Hwang, S.; Roh, J. W.; Ahn, K.; Yeon, D.-H.; Lee, K. H.; Kim, S. W. *Journal of Materials Research* **2012**, *27*, 2449–2456.
(31) Lin, Q.; Smeller, M.; Heideman, C. L.; Zschack, P.; Koyano, M.; Anderson, M. D.; Kykyneshi, R.; Keszler, D. A.; Anderson, I. M.; Johnson, D. C. *Chemistry of Materials* **2010**, *22*, 1002–1009.
(32) Mavrokefalos, A.; Lin, Q.; Beekman, M.; Seol, J. H.; Lee, Y. J.; Kong, H.; Pettes, M. T.; Johnson, D. C.; Shi, L. *Applied Physics Letters* **2010**, *96*, 181908.
(33) Zhang, Y.; Wang, H.; Krämer, S.; Shi, Y.; Zhang, F.; Snedaker, M.; Ding, K.; Moskovits, M.; Snyder, G. J.; Stucky, G. D. *ACS Nano* **2011**, *5*, 3158–3165.
(34) Sumithra, S.; Takas, N. J.; Misra, D. K.; Nolting, W. M.; Poudeu, P. F. P.; Stokes, K. L. *Advanced Energy Materials* **2011**, *1*, 1141–1147.
(35) Birkel, C. S.; Douglas, J. E.; Lettiere, B. R.; Seward, G.; Verma, N.; Zhang, Y.; Pollock, T. M.; Seshadri, R.; Stucky, G. D. *Physical Chemistry Chemical Physics* **2013**, *15*, 6990–7.
(36) Puneet, P.; He, J.; Zhu, S.; Tritt, T. M. *Journal of Applied Physics* **2012**, *112*, 033710
(37) Zhao, L.-D.; Zhang, B.-P.; Liu, W.-S.; Li, J.-F. *Journal of Applied Physics* **2009**, *105*, 23704–23706.
(38) Hsu, K. F.; Loo, S.; Guo, F.; Chen, W.; Dyck, J. S.; Uher, C.; Hogan, T.; Polychroniadis, E. K.; Kanatzidis, M. G. *Science* **2004**, *303*, 818–821.
(39) Kanatzidis, M. G. *Chemistry of Materials* **2010**, *22*, 648–659.
(40) Poudeu, P. F. P.; Guéguen, A.; Wu, C.-I.; Hogan, T.; Kanatzidis, M. G. *Chemistry of Materials* **2010**, *22*, 1046–1053.
(41) Liu, Y.; Sahoo, P.; Makongo, J. P. A.; Zhou, X.; Kim, S.-J.; Chi, H.; Uher, C.; Pan, X.; Poudeu, P. F. P. *Journal of the American Chemical Society* **2013**, *135*, 7486–95.
(42) Van Nong, N.; Pryds, N.; Linderoth, S.; Ohtaki, M. *Advanced Materials* **2011**, *23*, 2484–90.
(43) Han, M.-K.; Ahn, K.; Kim, H.; Rhyee, J.-S.; Kim, S.-J. *Journal of Materials Chemistry* **2011**, *21*, 11365-11370.
(44) Girard, S. N.; He, J.; Li, C.; Moses, S.; Wang, G.; Uher, C.; Dravid, V. P.; Kanatzidis, M. G. *Nano Letters* **2010**, *10*, 2825–31.
(45) Zhao, L.-D.; He, J.; Wu, C.-I.; Hogan, T. P.; Zhou, X.; Uher, C.; Dravid, V. P.; Kanatzidis, M. G. *Journal of the American Chemical Society* **2012**, *134*, 7902–12.
(46) Zhao, L.-D.; He, J.; Hao, S.; Wu, C.-I.; Hogan, T. P.; Wolverton, C.; Dravid, V. P.; Kanatzidis, M. G. *Journal of the American Chemical Society* **2012**, *134*, 16327–36.
(47) Biswas, K.; He, J.; Zhang, Q.; Wang, G.; Uher, C.; Dravid, V. P.; Kanatzidis, M. G. *Nature Chemistry* **2011**, *3*, 160–6.
(48) Ahn, K.; Han, M.-K.; He, J.; Androulakis, J.; Ballikaya, S.; Uher, C.; Dravid, V. P.; Kanatzidis, M. G. *Journal of the American Chemical Society* **2010**, *132*, 5227–35.
(49) Pei, Y.; Lensch-Falk, J.; Toberer, E. S.; Medlin, D. L.; Snyder, G. J. *Advanced Functional Materials* **2011**, *21*, 241–249.
(50) He, J.; Girard, S. N.; Kanatzidis, M. G.; Dravid, V. P. *Advanced Functional Materials* **2010**, *20*, 764-772
(51) Wang, W.; Goebl, J.; He, L.; Aloni, S.; Hu, Y.; Zhen, L.; Yin, Y. *Journal of the American Chemical Society* **2010**, *132*, 17316–24.
(52) Mehta, R. J.; Karthik, C.; Singh, B.; Teki, R.; Borca-Tasciuc, T.; Ramanath, G. *ACS Nano* **2010**, *4*, 5055–60.
(53) Ibanez, M.; Zamani, R.; Gorsse, S.; Fan, J.; Silvia, O.; Cadavid, D.; Morante, J. R.; Arbiol, J.; Cabot, A. *ACS Nano* **2013**, *7*, 2573–2586.
(54) Saramat, A.; Svensson, G.; Palmqvist, A. E. C. *Journal of Applied Physics* **2006**, *99*, 023708.
(55) Urban, J. J.; Talapin, D. V; Shevchenko, E. V; Kagan, C. R.; Murray, C. B. *Nature Materials* **2007**, *6*, 115–21.
(56) Mitzi, D. B.; Kosbar, L. L.; Murray, C. E.; Copel, M.; Afzali, A. *Nature* **2004**, *428*, 299–303.
(57) Mitzi, D. B. *Inorganic Chemistry* **2005**, *44*, 7078–86.
(58) Milliron, D. J.; Raoux, S.; Shelby, R. M.; Jordan-Sweet, J. *Nature Materials* **2007**, *6*, 352–6.
(59) Mitzi, D. *Inorganic Chemistry* **2007**, *46*, 926–931.
(60) Milliron, D. J.; Mitzi, D. B.; Copel, M.; Murray, C. E. *Chemistry of Materials* **2006**, *18*, 587–590.
(61) Kovalenko, M. V; Scheele, M.; Talapin, D. V. *Science* **2009**, *324*, 1417–20.

(62) Zhang, Y.; Snedaker, M. L.; Birkel, C. S.; Mubeen, S.; Ji, X.; Shi, Y.; Liu, D.; Liu, X.; Moskovits, M.; Stucky, G. D. *Nano Letters* **2012**, *12*, 1075–1080.
(63) Ko, D.-K.; Kang, Y.; Murray, C. B. *Nano Letters* **2011**, *11*, 2841–2844.
(64) Zhang, Y.; Bahk, J.-H.; Lee, J.; Birkel, C. S.; Snedaker, M. L.; Liu, D.; Zeng, H.; Moskovits, M.; Shakouri, A.; Stucky, G. D. in preparation for *Advanced Materials* **2013**.
(65) Small, J.; Perez, K.; Kim, P. *Physical Review Letters* **2003**, *91*, 256801.
(66) Yu, F.; Hu, L.; Zhou, H.; Qiu, C.; Yang, H.; Chen, M.; Lu, J.; Sun, L. *Journal of Nanoscience and Nanotechnology* **2013**, *13*, 1335–8.
(67) Bradley, K.; Jhi, S.; Collins, P.; Hone, J.; Cohen, M.; Louie, S.; Zettl, A. *Physical Review Letters* **2000**, *85*, 4361–4.
(68) Haskins, J.; Kinaci, A.; Sevik, C.; Sevincli, H.; Cuniberti, G.; Cagin, T. *ACS Nano* **2011**, *5*, 3779–3787.
(69) Yu, C.; Kim, Y. S.; Kim, D.; Grunlan, J. C. *Nano Letters* **2008**, *8*, 4428–32.
(70) Hewitt, C. A.; Kaiser, A. B.; Roth, S.; Craps, M.; Czerw, R.; Carroll, D. L. *Applied Physics Letters* **2011**, *98*, 183110.
(71) Choi, Y.; Kim, Y.; Park, S.-G.; Kim, Y.-G.; Sung, B. J.; Jang, S.-Y.; Kim, W. *Organic Electronics* **2011**, *12*, 2120–2125.
(72) Yao, Q.; Chen, L.; Zhang, W.; Liufu, S.; Chen, X. *ACS Nano* **2010**, *4*, 2445–2451.
(73) Wang, Q.; Yao, Q.; Chang, J.; Chen, L. *Journal of Materials Chemistry* **2012**, *22*, 17612-17618.
(74) Zhang, K.; Davis, M.; Qiu, J.; Hope-Weeks, L.; Wang, S. *Nanotechnology* **2012**, *23*, 385701.
(75) Liu, J.; Sun, J.; Gao, L. *Nanoscale* **2011**, *3*, 3616–9.
(76) Freeman, D. D.; Choi, K.; Yu, C. *PloS One* **2012**, *7*, e47822.
(77) Moriarty, G. P.; Wheeler, J. N.; Yu, C.; Grunlan, J. C. *Carbon* **2012**, *50*, 885–895.
(78) Kim, D.; Kim, Y.; Choi, K.; Grunlan, J. C.; Yu, C. *ACS Nano* **2010**, *4*, 513–523.
(79) Bounioux, C.; Díaz-Chao, P.; Campoy-Quiles, M.; Martín-González, M. S.; Goñi, A. R.; Yerushalmi-Rozen, R.; Müller, C. *Energy & Environmental Science* **2013**, *6*, 918-925.
(80) Kim, G. H.; Hwang, D. H.; Woo, S. I. *Physical Chemistry Chemical Physics* **2012**, *14*, 3530–6.
(81) Yu, C.; Choi, K.; Yin, L.; Grunlan, J. C. *ACS Nano* **2011**, *5*, 7885–92.
(82) Hewitt, C. A; Kaiser, A. B.; Roth, S.; Craps, M.; Czerw, R.; Carroll, D. L. *Nano Letters* **2012**, *12*, 1307–10.
(83) Fernandes, G. E.; Kim, J. H.; Xu, J. *Materials Research Bulletin* **2013**, *48*, 2950–2954.
(84) Yu, C.; Ryu, Y.; Yin, L.; Yang, H. *ACS Nano* **2011**, *5*, 1297–1303.
(85) Kim, K. T.; Choi, S. Y.; Shin, E. H.; Moon, K. S.; Koo, H. Y.; Lee, G.-G.; Ha, G. H. *Carbon* **2013**, *52*, 541–549.
(86) Suh, D.; Lee, D.; Kang, C.; Shon, I.-J.; Kim, W.; Baik, S. *Journal of Materials Chemistry* **2012**, *22*, 21376-21381.
(87) Zhang, Y.; Wang, X. L.; Yeoh, W. K.; Zheng, R. K.; Zhang, C. *Applied Physics Letters* **2012**, *101*, 031909.
(88) Tan, A.; Balachandran, J.; Sadat, S.; Gavini, V.; Dunietz, B. D.; Jang, S.-Y.; Reddy, P. *Journal of the American Chemical Society* **2011**, *133*, 8838–41.
(89) Bubnova, O.; Khan, Z. U.; Malti, A.; Braun, S.; Fahlman, M.; Berggren, M.; Crispin, X. *Nature Materials* **2011**, *10*, 429–33.
(90) See, K. C.; Feser, J. P.; Chen, C. E.; Majumdar, A.; Urban, J. J.; Segalman, R. A. *Nano Letters* **2010**, *10*, 4664–7.
(91) He, M.; Ge, J.; Lin, Z.; Feng, X.; Wang, X.; Lu, H.; Yang, Y.; Qiu, F. *Energy & Environmental Science* **2012**, *5*, 8351-8358.
(92) P. Goncalves, A.; Lopes, E. B.; Alves, E.; Barradas, N. P.; Franco, N.; Rouleau, O.; Godart, C. *New Approaches to Thermoelectric Materials. In Properties and Applications of Thermoelectric Materials*; Springer: Dordrecht, 2009; p. 51.

Yichi Zhang earned his bachelor's degree from Peking University in 2008. After being awarded his Ph.D. degree from University of California, Santa Barbara, in June 2013, he joined Dow Chemical Inc. He has published 19 scientific articles including four papers with first authorship. Honors include the Corning Fellowship (2010), Student Award at the 2nd Nano Today International Conference (2011), and the Excellence in Graduate Research Award at the 244th American Chemical Society Meeting (2012).

After earning his doctorate from Iowa State University in 1962, **Galen Stucky** held positions at the University of Illinois, Sandia, and DuPont before joining the faculty of the University of California, Santa Barbara, in 1985. He has published over 700 scientific articles and has been awarded 20 patents. Honors include the ACS Award in Chemistry of Materials (2002), the ATACCC Award (2008), and election to the National Academy of Sciences (2013).

SYNOPSIS TOC